Final version of this paper was published at
Sensors and Actuators A 352 (2023), 114201, https://doi.org/10.1016/j.sna.2023.114201

An eddy current speed sensor with a novel configuration of longitudinal and transversal coils

Mehran Mirzaei*, Pavel Ripka, and Vaclav Grim
Faculty of Electrical Engineering, Czech Technical University, Prague 16627, Czech Republic
** Corresponding author: mirzameh@fel.cvut.cz*

***Abstract*—This paper presents a novel eddy current speed sensor for linear speed measurement of moving flat iron part. The main goal of the paper is to present an efficient eddy current speed sensor with high sensitivity and fault-tolerant capability using novel configuration of pickup coils. It has one rectangular excitation coil and two sets of pickup coils for voltage measurement. The first set of pickup coils consists of eleven serially connected coils, which are perpendicularly mounted and arranged on top of the excitation coil in transversal direction. The second set of pickup coils comprises two antiserially connected pickup coils, which are located in the longitudinal direction as the excitation coil. The measurements of the sensor are performed up to ±17.9 m/s (64 km/h) at excitation frequencies 1000 Hz and 4000 Hz. Analytical calculations are used for the parametric and performance analyses of the eddy current speed sensor. The calculation results are compared with the measurements. The sensor nonlinearity error is 1 %. The performance of the sensor is also assessed for a higher speed range up to 600 km/h.**

***Index Terms*—Analytical, eddy current, linear speed measurement, longitudinal and perpendicular coils, speed sensor.**

I. INTRODUCTION

THE railway system is the most capable transportation system in terms of high energy efficiency and it is environmentally friendly [1]. The speed control is a key part in railway transportation systems [2]-[3]. The speed measurement systems in the railways can be categorized in two groups, which are direct and indirect methods. Indirect speed sensors are mounted or operated on the traction motors or wheelsets. They can be contactless or in contact with rotating shafts of traction motors or wheelsets.

Tachometers, variable reluctance [4], and optical sensors are convenient for railway speed measurements, and these are indirect methods and in contact configurations. The optical or magnetic saliency on a moving object is required. Rotating resolvers [5]-[6] are precise and cost effective for indirect speed measurements in the railways, which could be installed on the shaft of electrical traction motors or coupled to it [7]-[10]. However, indirect speed measurements are erroneous in rainy weather caused by slipping and sliding of the wheels on the iron rails. Also, the cost, complexity and vulnerability to the mechanical damages for in contact sensors, dust and dirt for the optical sensors are challenging issues.

Sensorless speed measurement is an indirect method with a nondestructive and mechanically contactless approach, which utilizes electrical signals of traction motors for the speed estimations [11]. However, it has complicated signal processing unit, and is less fault-tolerant against electrical failure in traction motors. Therefore, it can be less cost effective in terms of maintenance and repair.

Direct sensors for linear speed measurement in railway applications are microwave Doppler radar, accelerometers, GPS and correlation methods using two sensors for the speed measurement. Doppler radar speed sensor requires costly maintenance, and it is less reliable, prone to failure in rain and fog, while GPS availability is problematic in tunnels. Linear resolvers could measure directly the linear speed of the moving objects [12]-[13]. They are operated based on variable reluctance as rotating resolvers and they need magnetically salient part in the secondary side. However, they need long magnetically salient secondary part for the short primary (stator) part or long primary part for the short salient moving secondary part [14]. The long parts for primary or secondary must be mounted on the auxiliary third rail. Therefore, they are not practically and economically feasible for long distance railway applications.

Utilizing eddy currents is a nondestructive method in many electromagnetic applications [15]. Eddy current speed sensors in the railway track can be used for direct and indirect speed measurement. An indirect method to measure the railway speed using rotating permanent magnet cylinder was presented in [16], which is operated based on interaction of induced eddy current on the rails and rotating permanent magnet fields during the train movement. It is mechanically less fault tolerant because of rotating cylinder despite its nondestructive and contactless approach for the speed measurement. The induced eddy current has two components: 1- transformer component caused by AC excitation fields, 2- motional component caused by relative motion between conductive objects and excitation fields. Motional component of eddy current in the conductive objects cause asymmetrical magnetic flux distribution, which could be utilized for speed measurement of conductive objects. Electromagnetic and eddy current flowmeters operate based on utilization of motional component of eddy currents [17]-[18]. Eddy current speed sensors for direct measurements of linear speed of solid moving objects were developed in [19]-[23] for

only aluminum and nonmagnetic moving parts. The sensors in [19]-[22] have two antiserially longitudinal coils pickup coils or one perpendicular pickup coil. The presented sensor in [22] with rectangular coils and Ferrite yoke is similar to the one in [19] and it was tested for aluminum moving part. An eddy current speed sensor utilizing the forces caused by the motional component of the induced eddy current in an aluminum sheet developed in [23] was only tested up to 2.5 m/s, and it m has a complicated mechanical structure. The authors developed different configurations of linear eddy current sensors for speed measurement of iron and aluminum plates [24]-[28]. One pair of pickup coils or single pickup coil were used in [19] – [27]. Using only one set of pickup coils cause the sensor to be vulnerable to the mechanical or electrical fault in the pickup coils and corresponding signal processing unit. The eddy current speed sensor presented in [28] has two pairs of pickup coils, however, the sensitivity of second pair of pickup coils is considerably lower than the first one.

One novel structure of eddy current speed sensor is presented in this paper with two sets of pickup coils and one excitation coil with high sensitivity, compactness and fault tolerant capability. First and second set of pickup coils are positioned perpendicularly to the excitation coil and in longitudinal direction as the excitation coil, respectively. Increasing the number of pickup coils from one set in [19]-[22] and [24]-[27] to two sets in this paper and above improves the reliability of the sensor when, for example, one of pickup coils set or corresponding signal processing unit was mechanically damaged. The novel structure of pickup coils helps to reduce the length of the sensor where it is a space constraint. The performance analysis of eddy current speed sensor and its parametric calculations are presented using a 3D analytical method. The sensitivities of the sensor for both sets of pickup coils are sufficient to measure the speed of the moving magnetic objects. The sensitivities of the proposed sensor for the first and second sets pickup coils corresponding to the absolute value of sensor voltage are considerably improved in comparison with the first set of pickup coils of the speed sensor in [28]. For example, their ratios to the sensitivities in the sensor [28] in percentage are 278% and 98.5% with magnetic yoke and they are 754% and 267% without magnetic yoke.

II. Configuration of Eddy Current Speed Sensor

Fig. 1 shows 3D model of the eddy current speed sensor with moving part with speed, v in longitudinal x-direction. Eddy current sensor comprises one excitation coil and two sets of pickup coils as shown in Fig. 2 with transversal coils perpendicular to the excitation coil and in Fig. 3 with longitudinal coils accommodated inside the excitation coil.

The magnetic fields generated by the excitation coil current and transformer component of induced eddy current in the stationary conductive part are symmetric (Fig. 4 a)):
1-The induced voltage in the coil, 6 in first set in Fig. 2 is zero at $v = 0$. The induced voltages in the coils, 1 to 5 are equal to the voltage in the coils, 7 to 11 in magnitude but with opposite polarity. Therefore, the net voltage in 11 serially connected coils becomes zero.
2-The induced voltages in two coils of second set in Fig. 3 are equal in magnitude and polarity at $v = 0$. Therefore, the net output voltage is zero in antiserially connection of the coils.

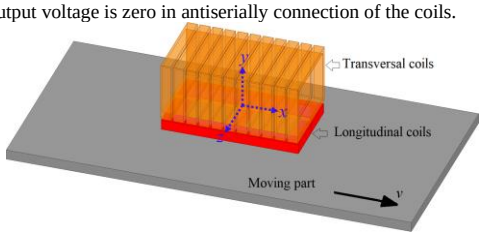

Fig. 1. 3D model of eddy current speed sensor and moving part, which is a ferromagnetic conductive plate or rail

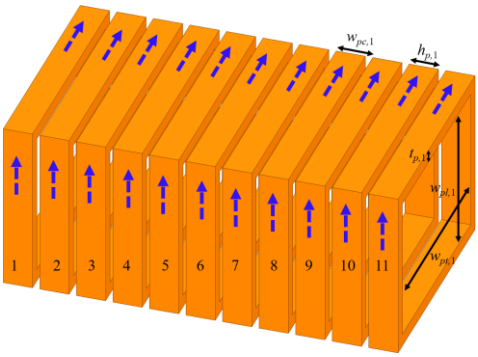

Fig. 2. Transversal coils for first set – eleven serially connected pickup coils

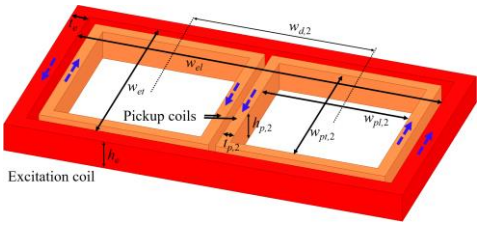

Fig. 3. Longitudinal coils for second set – a excitation coil that comprises two antiserially connected pickup coils

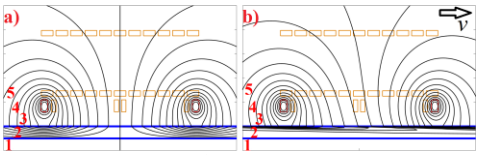

Fig. 4. Schematic 2D magnetic flux distributions in y-x plane - a) symmetric at zero speed, $v = 0$ and b) asymmetric at nonzero speed, $v \neq 0$

The motional component of eddy current is induced in the moving conductive part, which causes asymmetric magnetic field distribution (Fig. 4 b)). Therefore, the voltage is generated in both sets of pickup coils at $v \neq 0$. The generated voltage is proportional to the speed, which can be utilized as a speed

meter.

III. Modeling

Table I presents the parameters and dimensions of the proposed eddy current speed sensor according to Fig. 2 and Fig. 3. 3D analytical method is used for parametric calculations and theoretical performance analysis of the eddy current speed sensor using the parameters in Table I. Using 3D analytical method helps for precise and fast analyses.

TABLE I
Parameters and Dimensions of Eddy Current Speed Sensor

Parameter	Value
N_e: Number of turns in the excitation coil	200
$N_{p,1}$, $N_{p,2}$: Number of turns in each pickup coils	100
h_e: Height of excitation coil	5 mm
t_e: Thickness of excitation coil	2.85 mm
w_{te}: Inner width of excitation coil in trans. dir. (z-axis)	32 mm
w_{el}: Inner width of excitation coil in longt. dir. (x-axis)	62 mm
$h_{p,1}$: Height of pickup coils, 1	5 mm
$t_{p,1}$: Thickness of pickup coils, 1	2.25 mm
$w_{pt,1}$: Inner width of pickup coils, 1 in trans. dir. (z-axis)	35 mm
$w_{pl,1}$: Inner width of pickup coils, 1 in longt. dir. (x-axis)	25 mm
$w_{pc,1}$: Pitch of pickup coils, 1 in longt. dir. (x-axis)	6.25 mm
$h_{p,2}$: Height of pickup coils, 2	5 mm
$t_{p,2}$: Thickness of pickup coils, 2	1.9 mm
$w_{pt,2}$: Inner width of pickup coils, 2 in trans. dir. (z-axis)	25 mm
$w_{pl,2}$: Inner width of pickup coils, 2 in longt. dir. (x-axis)	25 mm
$w_{d,2}$: Distance between centers of pickup coils, 2	30 mm
g_m: Gap distance between moving part and excitation coil	6 mm, 8 mm
g_c: Gap distance between excitation and pickup coils, 1	1.5 mm
d: Thickness of moving part	5 mm

A. Theoretical Calculations

The Maxwell electromagnetic equations in differential forms are as follows:

$$\nabla \cdot B = 0 \;\rightarrow\; B = \nabla \times A$$
$$\nabla \times J = -\sigma \frac{\partial B}{\partial t},\ \nabla \cdot J = 0 \;\rightarrow J = \nabla \times S$$
$$\nabla \times H = J\ ,\quad B = \mu_r \mu_0 H \tag{1}$$

where, B, A, J, H, σ, μ_r are magnetic flux density, magnetic vector potential, current density, magnetic field strength, electrical conductivity and relative magnetic permeability. S is the streamline function.

The moving part is solid iron plate with relative magnetic permeability, μ_r. The x-component of magnetic vector potential, A_x in longitudinal direction and z-component of magnetic vector potential, A_z in transversal direction are only considered. The y-component of the magnetic vector potential is zero as the excitation coil is parallel to z-x plane according to Fig. 1. Coulomb gauge condition in (3) is assumed to obtain solutions for A_x and A_z. The differential equations in (2) are obtained using (1) and (2) versus A_x and A_z.

$$\nabla \cdot A = 0 \rightarrow \frac{\partial A_x}{\partial x} + \frac{\partial A_z}{\partial z} = 0 \tag{2}$$

$$\frac{\partial^2 A_x}{\partial x^2} + \frac{\partial^2 A_x}{\partial y^2} + \frac{\partial^2 A_x}{\partial z^2} = -\mu_r \mu_0 J_x$$
$$\frac{\partial^2 A_z}{\partial x^2} + \frac{\partial^2 A_z}{\partial y^2} + \frac{\partial^2 A_z}{\partial z^2} = -\mu_r \mu_0 J_z \tag{3}$$

The x- and z-components of the current densities J_x and J_z in (3) are zero for air regions shown in (4). They are equal to source current density, J_s in (5) for the excitation coil region. Equation (6) shows current densities used in (3) for the moving part [29], which represents eddy currents. I is the excitation coil current.

$$J_x = J_z = 0 \tag{4}$$

$$J_x = J_z = J_s, \qquad J_s = \frac{N_e \cdot I}{h_e \cdot t_e} \tag{5}$$

$$J_x = -\sigma\left(\frac{\partial A_x}{\partial t} + v \cdot \frac{\partial A_x}{\partial x}\right),\ J_z = -\sigma\left(\frac{\partial A_z}{\partial t} + v \cdot \frac{\partial A_z}{\partial x}\right) \tag{6}$$

The separation of variable method using Fourier series [30] is utilized to solve differential equations in (3). Five regions, r is considered to solve (3) according to Fig. 4. Regions, r =1, 2, 3, 4 and 5 are air part below moving part, moving part region, air part between moving part and excitation coil, excitation coil region and air part above excitation coil, respectively. The solutions ae presented in (7) using parameters in in (8) and (9). The constants C_1^r and C_2^r in (7) are obtained using boundary conditions between regions, r =1, 2, 3, 4 and 5 [24]-[25] and [30]. The parameter $A_s^{m,n}$ in (7) is presented in (9) for excitation coil region, r = 4 and it is zero for other regions.

$$A_z = \sum_m \sum_n (C_1^r \cdot e^{\gamma \cdot y} + C_2^r \cdot e^{-\gamma \cdot y} + A_s^{m,n}) \cdot e^{j(\omega t - p \cdot x - q \cdot z)}$$
$$A_x = -\sum_m \sum_n \frac{q}{p} (C_1^r \cdot e^{\gamma \cdot y} + C_2^r \cdot e^{-\gamma \cdot y} + A_s^{m,n}) \cdot e^{j(\omega t - p \cdot x - q \cdot z)} \tag{7}$$

$$\alpha = \sqrt{p^2 + q^2}\ ,\ \beta = \sqrt{\alpha^2 + j\mu_0 \mu_r \sigma(\omega - p \cdot v)}\ ,\ \omega = 2\pi f$$
$$p = m\frac{\pi}{l}, m = \pm 1, \pm 3, \cdots,\quad q = n\frac{\pi}{L}, n = \pm 1, \pm 3, \cdots \tag{8}$$

$$A_s^{m,n} = \frac{\mu_0 J_s^{m,n}}{\gamma^2}$$
$$J_s^{m,n} = 4\frac{j}{n\pi l} C_e \cdot J_s$$
$$C_e = \frac{1}{p+q} C_{e,1} - \frac{1}{p-q} C_{e,2}$$
$$C_{e,1} = \cos\left(p\frac{w_{el}}{2} + q\frac{w_{et}}{2} + (p+q)t_e\right) \cdot \sin\left((p+q)\frac{t_e}{2}\right)$$

$$C_{e,2} = \cos\left(p\frac{w_{el}}{2} - q\frac{w_{et}}{2} + (p-q)t_e\right)\cdot\sin\left((p-q)\frac{t_e}{2}\right) \quad (9)$$

The parameter, γ is equal to β for moving part region, $r = 2$ and it is equal to α for other regions. f is the frequency.

The parameters l in longitudinal direction and L in transversal direction in (8) are considered large sufficient until the magnetic fields become weak. They are considered about 1420 mm and 150 mm in this paper, according to the dimensions of the rotating disk used for the experimental testing. m, n in (8) are harmonic orders for Fourier analysis, which are odd numbers.

Equation (10) presents induced voltage equation in pickup coils $U_{p,1,2}$:

$$U_{p,1,2} = -j\omega\Psi_{p,1,2}\ ,\Psi_{p,1,2} = \frac{N_{p,1,2}\int\int A_{x,z}\cdot dl\, ds}{h_{p,1,2}\cdot t_{p,1,2}} \quad (10)$$

where $\Psi_{p,1,2}$ is the total average mutual flux linkage over the volume of the pickup coils. Line integration of A_x and A_z (dl) is applied to the pickup coils regions in the artificial current flow direction in the *y*-*z* plane for transversal coils [24] and the *z*-*x* plane for longitudinal coils [25]. The line integral is considered only in the *z*-direction of the coil sides. The surface integration (ds) in (10) is performed over the pickup coil cross-section area, which is averaged over the coil cross-section area, $h_{p,1,2}\cdot t_{p,1,2}$.

Equations (11) and (12) using (13)-(14) present formulas for the induced voltages using the parameters in Table I for the first set of transversal pickup coils in Fig. 2, $U_{p,1}$ and second set of longitudinal pickup coils in Fig. 3, $U_{p,2}$, respectively.

$$U_{p,1} = -8\omega\frac{N_{p,1}}{h_{p,1}\cdot t_{p,1}}\sum_m\sum_n\frac{1}{p\cdot q}\sin\left(p\frac{h_{p,1}}{2}\right)U_0^{m,n}\,C_{p,1}\cdot C_w$$

$$C_w = \frac{\sin\left(p\frac{11\cdot w_{pc,1}}{2}\right)}{\sin\left(p\frac{w_{pc,1}}{2}\right)}$$

$$U_0^{m,n} = C_{2,r_3}e^{-\gamma w_{d,1}}$$

$$w_{d,1} = g_m + h_{e,p} + g_c + t_{p,1} + \frac{w_{pl,1}}{2}$$

$$C_{p,1} = \frac{1}{q}\cdot\left(\frac{1}{j\gamma+q}C_{p,1,1} - \frac{1}{j\gamma-q}C_{p,1,2}\right)$$

$$C_{p,1,1} = \cos\left(j\gamma\frac{w_{pl,1}}{2} + q\frac{w_{pt,1}}{2} + (j\gamma+q)\frac{t_{p,1}}{2}\right)\sin\left((j\gamma+q)\frac{t_{p,1}}{2}\right)$$

$$C_{p,1,2} = \cos\left(j\gamma\frac{w_{pl,1}}{2} - q\frac{w_{pt,1}}{2} + (j\gamma-q)\frac{t_{p,1}}{2}\right)\sin\left((j\gamma-q)\frac{t_{p,1}}{2}\right) \quad (11)$$

$$U_{p,2} = -2\omega\frac{N_{p,2}\cdot L\cdot l}{h_{p,2}\cdot t_{p,2}}\sum_m\sum_n\left(1+\frac{q^2}{p^2}\right)U_1^{m,n}\,C_{p,2}\cdot\sin\left(p\frac{w_{d,2}}{2}\right),\qquad \omega = 2\pi f$$

$$C_{p,2} = 4\frac{j}{n\pi l}\cdot\left(\frac{1}{p+q}C_{p,2,1} - \frac{1}{p-q}C_{p,2,2}\right)$$

$$C_{p,2,1} = \cos\left(p\frac{w_{pl,2}}{2} + q\frac{w_{pt,2}}{2} + (p+q)\frac{t_{p,2}}{2}\right)\sin\left((p+q)\frac{t_{p,2}}{2}\right)$$

$$C_{p,2,2} = \cos\left(p\frac{w_{pl,2}}{2} - q\frac{w_{pt,2}}{2} + (p-q)\frac{t_{p,2}}{2}\right)\sin\left((p-q)\frac{t_{p,2}}{2}\right)$$

$$U_1^{m,n} = -\frac{C_{2,r_3}}{\gamma}\left(e^{-\gamma(g_m+h_{p,2})} - e^{-\gamma g_m}\right) \quad (12)$$

$$C_{2,r_3} = \frac{\mu_r\cdot\gamma - K'}{\mu_r\cdot\gamma + K'}C_{1,s_1}$$

$$C_{1,s_1} = \frac{\mu_0 J_s^{m,n}}{\gamma^2}e^{-\gamma\left(g_m+\frac{h_e}{2}\right)}\sinh\left(\gamma\frac{h_e}{2}\right) \quad (13)$$

$$K = \frac{\lambda+\mu_r\cdot\gamma}{\lambda-\mu_r\cdot\gamma}e^{2\lambda\cdot d},\quad K' = \lambda\frac{K-1}{K+1} \quad (14)$$

The eddy current distribution on the surface of moving iron part (*z*-*x* plane) using streamline function, S is shown in Fig. 5, which is drawn by equi-value streamlines, S. It shows asymmetric shape due to the speed effect. The streamline function is calculated using (1) and (6), $S_y = -\int J_x dz = \int J_z dx$. Fig. 6 depicts 2D magnetic flux distribution in midplane (*y*-*x* plane) of the sensor and in the longitudinal view. Magnetic flux lines are drawn using equipotential values of *z*-component of magnetic potential, A_z in *y*-*x* plane ($z = 0$) in middle plane of the sensor where, $A_x = 0$ because of sensor symmetry in *z*-direction.

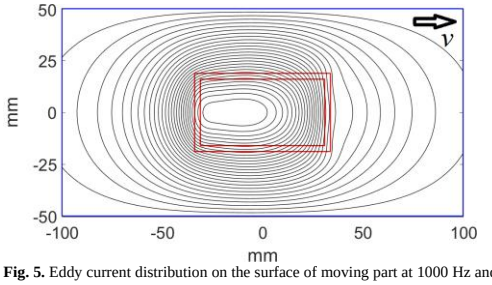

Fig. 5. Eddy current distribution on the surface of moving part at 1000 Hz and speed, v = +17.9 m/s – σ = 6 MS/m and μ_r = 100

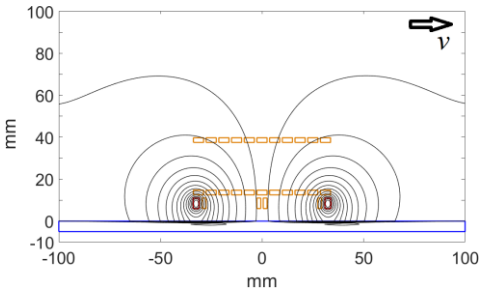

Fig. 6. 2D magnetic flux distribution at 1000 Hz and speed, v = +17.9 m/s – σ = 6 MS/m and μ_r = 100

B. Parametric Analysis

The parametric calculations are performed to evaluate the effects of the excitation frequency and the material properties of moving iron part on the sensor performance. The analytically calculated voltage of first set with transversal coils and second set with longitudinal coils are presented. The eddy current speed sensor operates at low magnetic fields. Therefore, the relative magnetic permeability, μ_r is considered about 100, which is close to the initial permeability of solid irons and steels.

The curves of real, $U_{p,r}/I$ and imaginary $U_{p,i}/I$ components of voltage to excitation current ratio versus frequency are presented in Fig. 7 up to 10000 Hz. The calculated real and imaginary components of the voltage to current ratio are in phase and quadrature phase with excitation coil current. The real component of voltage to current ratio, $U_{p,r}/I$ is higher than imaginary component, at higher frequencies f > 100 Hz. It has maximum value at 5600 Hz. The real and imaginary components of flux linkages to current ratio versus frequency are depicted in Fig. 8. The curve of real component of flux linkage to current ratio shows a maximum value at 100 Hz. The curve of imaginary component of flux linkage to current ratio has constant part at low frequencies, f< 50 Hz and it decreases monotonically at higher frequencies due to the skin effect.

The effects of conductivity σ and relative magnetic permeability μ_r of moving iron part on the performance of eddy current speed sensor are evaluated in Fig. 9 and Fig. 10 at 1000 Hz and 4000 Hz. The calculations of the voltage to current ratio are performed for conductivity range, 1 – 10 MS/m and relative magnetic permeabilities of 50, 100 and 150. The real component of voltage to current ratio is higher for lower value of μ_r = 50 except for higher conductivities at 4000 Hz. It is contrariwise for imaginary component of voltage to current ratio, which is lower for lower permeabilities. The real component of voltage is less sensitive to the relative magnetic permeability at 4000 Hz at conductivity range σ > 4 MS/m, which is the case for most industrial irons and steels; for example, iron rails have conductivity above 4 MS/m at different environment temperatures.

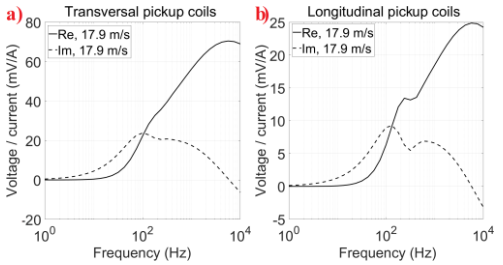

Fig. 7. The real (Re) and imaginary (Im) components of voltage to current ratio versus frequency, g_m = 6 mm, σ = 6 MS/m and μ_r = 100 – a) first set of pickup coils, b) second set of pickup coils (analytical)

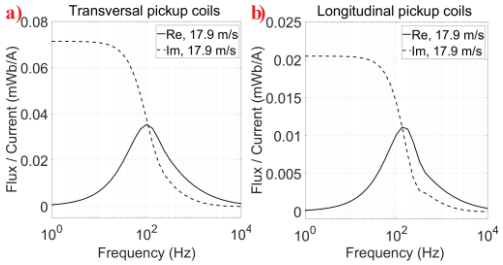

Fig. 8. The real (Re) and imaginary (Im) components of flux linkage to current ratio versus frequency, g_m = 6 mm, σ = 6 MS/m and μ_r = 100– a) first set of pickup coils, b) second set of pickup coils (analytical)

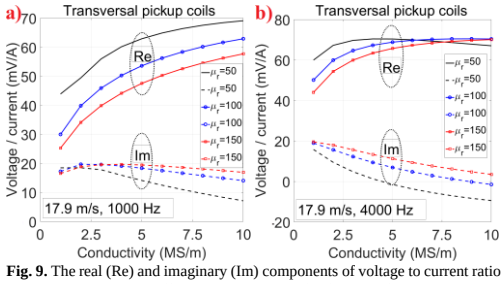

Fig. 9. The real (Re) and imaginary (Im) components of voltage to current ratio versus conductivity at different μ_r, g_m = 6 mm for first set of pickup coils – a) 1000 Hz, b) 4000 Hz (analytical)

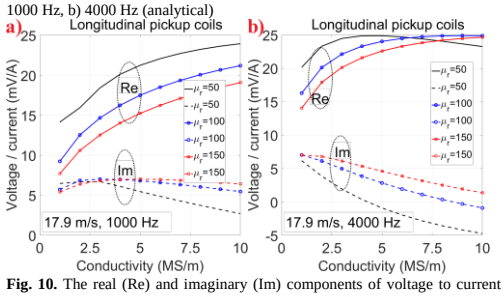

Fig. 10. The real (Re) and imaginary (Im) components of voltage to current ratio versus conductivity at different μ_r, g_m = 6 mm for second set of pickup coils – a) 1000 Hz, b) 4000 Hz (analytical)

IV. Experiments

Fig. 11 shows the experimental setup for eddy current speed sensor using a solid iron rotating disc as a moving part. The coils in the tested sensor are shown in Fig. 12. The rotating disc with external diameter 55.5 cm is considerably larger than the sensor to model linear motion as shown in Fig. 1. The distance between the sensor center and rotating disc, r_s is 22.75 cm as shown in Fig. 11. The iron disc is rotated by a DC motor controlled by the armature voltage, which rotating speed, n_r in rpm is measured by a reference sensor. The reference sensor is an absolute angle sensor based on dual GMR bridge, type TLE5012, made by Infineon Technology to measure magnetic fields of NdFeB magnet placed on the rear shaft of the DC motor. The output of the sensor is 1 pulse per revolution digital signal; itsfrequency f_r (= n_r/60) is measured with a frequency counter Agilent 53131A. The linear speed of moving part can be calculated $v = r_s \cdot 2\pi \cdot n_r/60$

The schematic view for experimental setup for the sensor voltages measurement is shown in Fig. 13. The excitation coil with resistance 29.7 Ω in series with an external resistance 9 Ω, which are connected to a signal generator with voltage amplitude 10 V and internal resistance 50 Ω. The voltage across the external resistance is measured, which indicates excitation coil current. Each set of the pickup coils is connected to the Lock-in Amplifier, Stanford Research System, model SR830 DSP to measure real and imaginary components of induced voltages. The real and imaginary components of the voltage are measured relative to the excitation coil current as reference signal. The measured currents of the excitation coil at 1000 Hz and 4000 Hz are presented in Table II for two mechanical gaps, g_m = 6 mm and 8 mm. They were measured using voltage across external resistance, R = 9 Ω shown in Fig. 13. The measured current is lower at 4000 Hz in comparison with 1000 Hz and source voltage amplitude, 10 V as the reactance of excitation coil becomes higher.

TABLE II
The Measured Current of The Speed Sensor

The voltage amplitude of signal generator is 10 V		*I*	
		1000 Hz	4000 Hz
Excitation coil current	g_m = 6 mm	74.9 mA	48.4 mA
	g_m = 8 mm	75.3 mA	49.2 mA

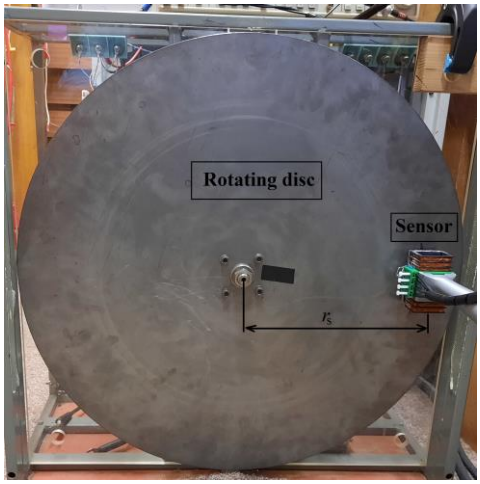

Fig. 11. The eddy current speed sensor and rotating disc as a moving magnetic conductive object

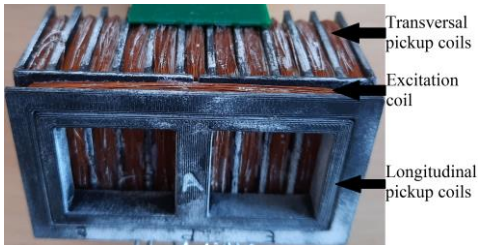

Fig. 12. The coils of the eddy current speed sensor – transversal pickup coils, excitation coil and longitudinal pickup coils accommodated in inner space of excitation coil

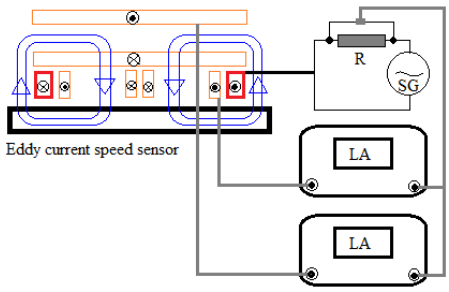

Fig. 13. Schematic view of eddy current speed sensor with measurement elements: lock-in amplifier (LA), signal generator (SG), and external resistance (R)

A. *Experimental Results*

The sensor voltages versus time at excitation frequencies, 1000 Hz and 4000 Hz are shown in Fig. 14. The sensor voltages are lower at 4000 Hz as the excitation current is lower as presented in Table II. The voltages for transversal coils

are about 2.7-times higher in comparison with longitudinal coils.

TABLE III
THE SENSITIVITIES OF THE SPEED SENSOR

(mV/(m/s·A))		K_r		Ki	
		1000 Hz	4000 Hz	1000 Hz	4000 Hz
First set - transversal coils	6 mm	2.81	3.64	1.07	0.72
	8 mm	2.34	2.92	0.83	0.53
Second set - longitudinal coils	6 mm	0.96	1.37	0.46	0.36
	8 mm	0.77	0.95	0.28	0.04

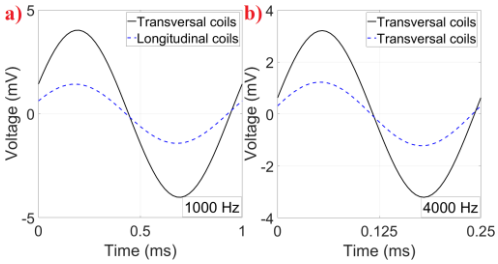

Fig. 14. The voltage versus time, g_m = 6 mm, v = +17.9 m/s – a) 1000 Hz and I = 74.9 mA, b) 4000 Hz and I = 48.4 mA (measurement)

Fig. 15 and Fig. 16 show the curves of the measured real, $U_{p,r}$ and imaginary, $U_{p,i}$ components of voltage to current ratio versus speed for two mechanical gaps, g_m = 6 mm and 8 mm at 1000 Hz and 4000 Hz. They show high linearity characteristics with nonlinearity error about 1 %, which shows the suitability of the sensor for the linear speed measurement. The real component is higher and imaginary component is lower at 4000 Hz in comparison with corresponding values at 1000 Hz.

Table III presents the sensitivity of the eddy current speed sensor for two sets of pickup coils corresponding to real, $K_r = U_{p,r}/(I \cdot v)$ and imaginary, $K_i = U_{p,i}/(I \cdot v)$ components of voltage corresponding to Fig. 15 and Fig. 16. The sensitivities in the first set of pickup coils are 100% to 200% higher in comparison with second set of pickup coils. With increasing frequency from 1000 Hz to 4000 Hz, the K_r increases by 23% - 43% and the K_i decreases by 22% - 36%. With 33% increasing of the gap between moving iron part and coils, g_m from 6 mm to 8 mm, the K_r decreases between 17% to 30%. The change of K_r is higher at higher frequencies for changing of gap. The K_i is more sensitive to the gap changing and it decreases about 40 % for 33% increasing gap.

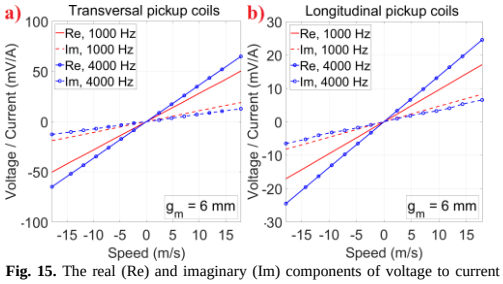

Fig. 15. The real (Re) and imaginary (Im) components of voltage to current ratio versus speed, g_m = 6 mm – a) first set of pickup coils, b) second set of pickup coils (measurement)

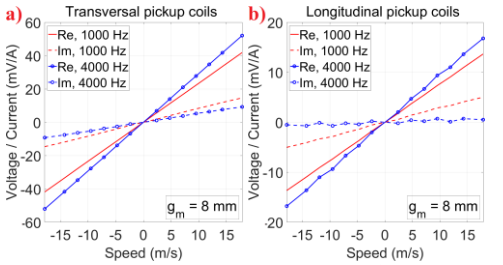

Fig. 16. The real (Re) and imaginary (Im) components of voltage to current ratio versus speed, g_m = 8 mm – a) first set of pickup coils, b) second set of pickup coils (measurement)

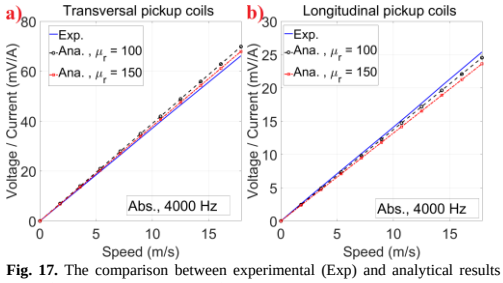

Fig. 17. The comparison between experimental (Exp) and analytical results (Ana) for absolute (Abs) value of voltage to current ratio versus speed, g_m = 6 mm, σ = 6 MS/m and μ_r = 100 – a) first set of pickup coils, b) second set of pickup coils

B. Comparison Between Experimental and Theoretical Results

The comparison between theoretical and experimental results are presented in Fig. 17 at 4000 Hz for absolute value of the voltage, $U_{p,a} = \sqrt{U_{p,r}^2 + U_{p,i}^2}$ to current ratio versus speed, which shows adequate accuracy of the analytical modeling. The errors for analytical and theoretical results in comparison with measurements are about 2.5% for the first set with transversal coils and 3.2% for the second set with longitudinal coils. Therefore, 3D analytical modeling could be used for further optimization of the speed sensor in terms of enhancing sensitivity and improving compactness. Evaluation of the sensor performance at higher speed ranges, for example, v > 100 km/h can be performed using 3D analytical method.

Realization of the experiments for the sensor at higher speeds is not cost effective because of mechanical complexity of the moving part. Therefore, the sensor performance can be assessed using a precise and fast 3D analytical method.

V. HIGHER SPEEDS OPERATION

Fig. 18 shows the sensor voltages to current ratio versus speed for higher range up to 600 km/h. The excitation frequency is selected 10000 Hz to achieve high linearity for the sensor voltage at higher speed operation. The corresponding sensitivity values are presented in Table IV. The K_i is negligible in comparison with K_r as imaginary component of the sensor voltage at 10000 Hz is considerably smaller in comparison with

real component of the sensor voltage. The sensitivity of transversal coils in first set is 187% higher than longitudinal coils in the second set, however, both set of pickup coils show appropriate sensitivity for high speed range and high excitation frequency. The results show that the proposed sensor can be utilized for low and high speed railways.

Real component of voltage is corresponding to the eddy current losses in moving conductive object. Imaginary component of voltage is corresponding to inductive coupling between excitation coil and pickup coils. The fields of induced eddy current at higher frequencies, 10000 Hz becomes stronger in comparison with source field of excitation coil and therefore, K_i becomes negative.

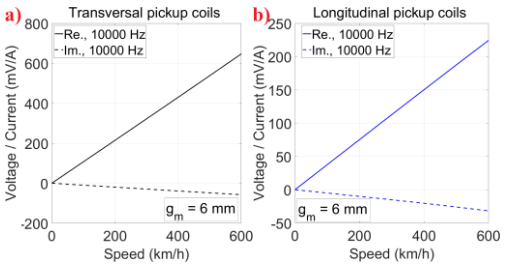

Fig. 18. The absolute value of voltage to current ratio versus speed up to 600 km/h, g_m = 6 mm σ = 6 MS/m and μ_r = 100 – a) first set of pickup coils, b) second set of pickup coils (analytical)

TABLE IV
THE SENSITIVITIES OF THE SPEED SENSOR AT HIGHER SPEEDS

mV/(m/s·A)		K_r	K_i
		10000 Hz	10000 Hz
First set - transversal coils	6 mm	3.88	-0.35
Second set - longitudinal coils	6 mm	1.35	-0.19

VI. DISCUSSIONS

Implementing 11 separate coils in the first set helps to increase their manufacturing accuracy. It also helps to increase set number of pickup coils. Fig. 19 shows the voltage to current ratio versus speed for different alternative configurations:

1) Fig. 19 a) compares the sensitivities when 11 pickup coils in Fig. 2 are in series in comparison to lower number of coils. The coils set is always symmetrical: for example, the coils 1 and 11 in Fig. 2 are excluded in 9-coils configuration. The middle coil 6 is only used for single coil arrangement in Fig. 19 a).

2) Fig. 19 b) shows another arrangement for transversal pickup coils. The voltage of single middle coil, 6 is compared with the voltage of series connections of couple coils of 5 and 7, 4 and 8, 3 and 9, 2 and 10 and finally 1 and 11, which are symmetrically located around he middle coil 6.

Therefore, it is concluded that more set of pickup coils could be extracted from second set of transversal pickup coils.

Increasing sensor output signals with adding more sets of pickup coils helps to improve speed sensor reliability and fault tolerant capability against electrical faults and mechanical damages, which can be occurred in the pickup coils and their signal processing units (SPU). Also, more output signals from the measurement can be further used for temperature and lift off compensation [31]. The sensor structure does not become complicated as each set of pickup coils are physically and electrically isolated with one SPU for each set. Using lock-in amplifier in SPU is an efficient method to extract very small signal from noise. Finally, the sensor can be magnetically shielded to protect sensor further against low and high frequency external signals and magnetic objects.

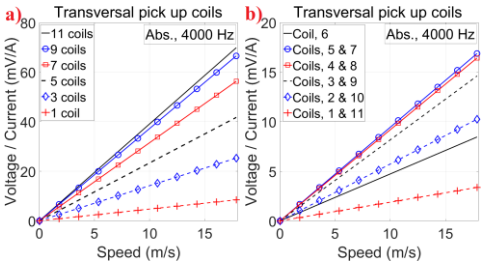

Fig. 19. Absolute (Abs) value of voltage to current ratio versus speed, g_m = 6 mm, σ = 6 MS/m and μ_r = 100 for transversal pick up coils– a) first alternative arrangement, b) first alternative arrangement (analytical)

The sensor presented in this paper was improved and optimized in comparison with sensors developed in [24]-[28]. The sensor in [25] was operated at low speeds below 2 m/s. The simulations results show that sensitivity corresponding to the transversal coils for presented sensor is about 2.6-times higher in comparison with the developed sensor in [24] at 360 Hz and it is 2.7-times higher in comparison with the sensor in [27] at 300 Hz. The sensitivity of the sensor in [26] is high, because it has ferrite core with high number of turns in the coils, which limits operation of the sensor at higher frequencies, f > 1000 Hz due to the high reactance value of the excitation coil an high parasitic capacitance of the pickup coils.

VI. CONCLUSION

A novel configuration of eddy current speed sensor was presented for linear speed measurements of industrial applications, for example, moving conductive ferromagnetic plates and iron rails. Longitudinal and perpendicular pickup coils were used to measure the induced voltage generated by motional component of induced eddy currents in solid iron moving plates. An exact 3D analytical method was used for parametric analysis and performance analysis of the sensor for low and high speed operations.

Implementing the second set of pickup coils help to improve the reliability and fault tolerant capability of the sensor and making the speed sensor more fault tolerant. It can be also applied for the compensation of the gap variations and for temperature compensation.

REFERENCES

[1] D. Ronanki, S. A. Singh, and S. S. Williamson, "Comprehensive Topological Overview of Rolling Stock Architectures and Recent Trends in Electric Railway Traction Systems," *IEEE Trans. Transp. Electrif.*, vol. 3, no. 3, pp. 724-738, Sept. 2017

Okomentoval(a): [PR1]: I do not understand this sentence. Maybe it can be removed,

[2] Z. Xiao, Q. Wang, P. Sun, B. You, and X. Feng, "Modeling and energy-optimal control for high-speed trains," *IEEE Trans. Transp. Electrif.*, vol. 6, no. 2, pp. 797-807, June 2020

[3] X.-H. Zhao, B.-R. Ke, and K.-L. Lian, "Optimization of train speed curve for energy saving using efficient and accurate electric traction models on the mass rapid transit system," *IEEE Trans. Transp. Electrif.*, vol. 4, no. 4, pp. 922-935, Dec. 2018

[4] T. Addabbo et al., "Instantaneous rotation speed measurement system based on variable reluctance sensors for torsional vibration monitoring", *IEEE Trans. Instrum. & Meas.*, vol. 68, no. 7, pp. 2363-2373, Jul. 2019

[5] M. S. KhajueeZadeh, H. Saneie, Z. Nasiri-Gheidari, "Development of a hybrid reference model for performance evaluation of resolvers," *IEEE Trans. Instrum. & Meas.*, vol. 70, 9004008, 2021

[6] A. Paymozd, H. Saneie, A. Daniar, and Z. Nasiri-Gheidari, "Accurate and fast subdomain model for electromagnetic design purpose of wound-field linear resolver," *IEEE Trans. Instrum. & Meas.*, vol. 70, 9003408, May 2021

[7] N. Zhao, and N. Schofield, "An induction machine design with parameter optimization for a 120-kW electric vehicle," *IEEE Trans. Transp. Electrif.*, vol. 6, no. 2, pp. 592-601, June 2020

[8] S. Zuo, X. Hu, D. Li, Yu Mao, Z. Wu, and Y. Xiong, "Analysis and suppression of longitudinal vibration of electric wheel system considering rotor position error," *IEEE Trans. Transp. Electrif.*, vol. 7, no. 2, pp. 671-682, June 2021

[9] C. Hong, W. Huang, and Z. Hu, "Design and analysis of a high-speed dual stator slotted solid-rotor axial-flux induction motor," *IEEE Trans. Transp. Electrif.*, vol. 5, no. 1, pp. 71-79, March 2019

[10] E. Libbos, B. Ku, S. Agrawal, S. Tungare, A. Banerjee, and P. T. Krein, "Loss minimization and maximum torque-per-ampere operation for variable-pole induction machines," *IEEE Trans. Transp. Electrif.*, vol. 6, no. 3. pp. 1051-1064, Sept. 2020

[11] M. Meira, G. R. Bossio, C. J. Verucchi, C. R. Ruschetti, and J. M. Bossio, "Speed estimation during the starting transient of induction motors," *IEEE Trans. Instrum. & Meas.*, vol. 70, 9000108, 2021

[12] R. Faryadras and F. Tootoonchian, "Design and experimental investigation of a two-DOF planar resolver," *IEEE Trans. Instrum. & Meas.*, vol. 71, 9000408, Dec. 2021

[13] P. Naderi, A. Ramezannezhad, and L. Vandevelde, "A novel linear resolver proposal and its performance analysis under healthy and asymmetry air-gap fault," *IEEE Trans. Instrum. & Meas.*, vol. 71, 9504109, March 2022

[14] F. Cui, Z. Sun, W. Xu, H. Qian, and C. Cao, "Optimization analysis of long primary permanent magnet linear synchronous motor," *IEEE Trans. Appl. Supercon.*, vol. 31, no. 8, 0603504, Nov. 2021

[15] W. Zhang, H. Sun, A. Tao, Y. Li, and Y. Shi, "Local defect detection of ferromagnetic metal casing based on pulsed eddy current testing," *IEEE Trans. Instrum. & Meas.*, vol. 71, 6003109, 2022

[16] C. Gong, A. Tuysuz, M. Flankl, T. Stolz, J. Kolar, and T. Habetler "Experimental analysis and optimization of a contactless eddy-current based speed sensor for smooth conductive surfaces," *IEEE Trans. Indus. Electro.*, vol. 67, no. 2, pp. 8817 - 8828, Oct 2020

[17] J.A. Shercliff, *The Theory of Electromagnetic Flow Measurement*, Cambridge University Press, 1962

[18] C. C. Feng, W. E. Deeds, and C. V. Dodd, "Analysis of eddy-current flowmeters," *J. Appl. Phys.*, vol. 46, pp. 2935-2940, 1975

[19] N. Takehira, A. Tanaka and K. Toda, "Analysis of a speed-meter utilizing eddy current effect", *Trans. Inst. Electron. Eng. Jpn. A*, vol. 97, no. 9, pp. 457-464, Sep. 1977

[20] N. Takehira and A. Tanaka, "Analysis of a perpendicular-type eddy-current speed meter," *IEE Proc. A (Phys. Sci., Meas. & Instrum., Manag. & Educ., Rev.)*, vol.135, no.2, pp. 89-94, Feb 1988.

[21] K. Ishida, T. Itaya T, A. Tanaka A and N. Takehira, "Exact analysis of a linear velocity sensor", *IEEE Trans. Instrum. & Meas.*, vol. 70, Oct. 2021

[22] A. Tuysuz, et al, "Three-dimensional analytical modeling of an eddy-current-based non-contact speed sensor," *IEEE Open J. of Ind. Appl.*, vol. 2, pp. 224-234, 2021

[23] A. Onat and S. Markon, "Theoretical and experimental analysis of eddy current contactless speed sensors for linear motor elevators," *IEEE Sens. J.*, vol. 22, no. 7, pp. 6345-6352, 2022

[24] M. Mirzaei, and P. Ripka, "A linear eddy current speed sensor with a perpendicular coils configuration," *IEEE Trans. Veh. Tech.*, vol. 70, no. 4, pp. 3197 - 3207, April 2021

[25] M. Mirzaei, P. Ripka, A. Chirtsov, J. Vyhnanek, and V. Grim, "Design and modeling of a linear speed sensor with a flat type structure and air coils," *J. Magn. & Magn. Mat.*, vol. 495, 165834, 1 February 2020

[26] M. Mirzaei, P. Ripka, and V. Grim, "A novel eddy current speed sensor with a Ferrite E-core," *IEEE Magn. Lett.* , vol. 11, 8102905, 08 May 2020

[27] M. Mirzaei, P. Ripka, A. Chirtsov, and V. Grim, "Eddy current speed sensor with magnetic shielding," *J. Magn. & Magn. Mat.*, vol.502, 166568, May 2020.

[28] M. Mirzaei, P. Ripka, and V. Grim, "A linear eddy current speed sensor for speed measurement of magnetic and nonmagnetic conductive objects," *13th Int. Symp. Linear Drives for Ind. Appl. (LDIA)*, Wuhan, China, 1-3 July 2021

[29] K. Yoshida, "New transfer-matrix theory of linear induction machines, taking into account longitudinal and transverse ferromagnetic end effects," *IEE Proceedings B – Elect. Power Appl.*, vol. 128 , no. 5, pp. 225-236, Sept. 1981

[30] K.J. Binns, P.J. Lawrenson, and C.W. Trowbridge, *The Analytical and Numerical Solutions of Electric and Magnetic Fields*, Published by John Wiley & Sons Ltd., 1992

[31] S. Zhu , R. Huang , J. R. S. Avila, Y. Tao, Z. Zhang, Q. Zhao, A. J. Peyton, and W. Yin, "Simultaneous measurements of wire diameter and conductivity using a combined inductive and capacitive sensor," *IEEE Sensors J.*, vol. 20, no. 19, pp. 11617-11624, Oct. 2020